Coherent two-exciton dynamics measured using two-quantum rephasing two-dimensional electronic spectroscopy

Daniel B. Turner,* Patrick Wen, Dylan H. Arias, and Keith A. Nelson†
Department of Chemistry, Massachusetts Institute of Technology, Cambridge, Massachusetts 02139, USA
(Received 5 October 2011; published 21 October 2011)

We use fifth-order two-dimensional electronic spectroscopy to measure coherent four-particle dynamics in a semiconductor nanostructure. By using optical polarization control in two-quantum measurements enabled by the COLBERT spectrometer, we separate coherent signals due to bound biexcitons and unbound two-exciton correlations. The rephasing nature of the measurement allows us to separate homogeneous from inhomogeneous contributions to the two-quantum line shapes. We find that, unlike the bound biexciton state, the energy of the unbound pair and its homogeneous linewidth depend on the laser fluence. Simulations using an extended phenomenological model help determine the primary interaction mechanism that leads to the formation of the unbound exciton pair; the model also indicates that seventh-order interactions contribute to the measured spectra under high pulse fluences.

DOI: 10.1103/PhysRevB.84.165321 PACS number(s): 78.67.De, 42.50.Md, 78.47.jh, 81.07.St

I. INTRODUCTION

Excitons are bound electron-hole pairs with wave functions somewhat similar to those of hydrogen atoms;[1–3] their resonances are the primary features in the optical spectra of semiconductor nanostructures at temperatures below the exciton binding energy. Exciton dynamics in direct-gap semiconductors are often studied using ultrafast spectroscopy because exciton correlations typically decay within a few picoseconds.[4] Phase-coherent nonlinear spectroscopic measurements such as four-wave-mixing are sensitive to the changes that occur when excitons interact through Coulomb forces[5] or local fields.[6] Early nonlinear "self-diffraction" measurements revealed a signal at "negative" delays due to many-body interactions (MBIs),[6–8] but since the exciton coherence frequencies could not be correlated with the emitted coherence frequencies, the contributions due to MBIs such as excitation-induced dephasing (EID),[9] excitation-induced energy shift (EIS),[10] and local-field effects (LFEs)[6] could not be distinguished. EID and EIS result in density-dependent collisional broadening and renormalization of the exciton energy, respectively. These experiments also could not distinguish these effects from bound biexcitons, and they did not contain phase information, which is an important distinguishing characteristic. In a significant advance, exciton correlations were observed using two-dimensional Fourier-transform optical spectroscopy (2D FTOPT). The correlations between exciton coherences induced by the first field interaction with the sample and exciton coherences that radiated phase-matched signals after two additional field interactions—meaning between one-quantum absorption and emission coherences—in the complex 2D spectra collected through optically heterodyned third-order four-wave-mixing revealed features due to many-body interactions.[11–13]

All of these MBIs can cause the motions of two excitons—four charged particles—to be correlated. This can result in a correlation between a pair of excitons without a binding energy (an unbound two-exciton correlation or UTC) or in the formation of a weakly bound state called a biexciton. The properties of biexcitons—first observed in GaAs quantum wells through biexciton-exciton emission[14]—are of substantial interest in connection with applications including optical gain.[15] A two-quantum variant of the 2D FTOPT measurement can measure two-exciton correlations directly. Recent improvements in the phase stabilization of multiple optical beams[16–19] enabled two-quantum 2D FTOPT measurements of both biexciton and UTC coherences in GaAs.[17–21] In this type of 2D FTOPT experiment, two-quantum coherence frequencies generated by the first two field interactions with the sample were correlated with the one-quantum coherence frequencies measured in the emitted signal induced by the third field interaction. This allowed the measurement of the binding energies and dephasing dynamics of biexcitons. The four-beam, square phase-matching geometry (often called the BOXCARS geometry) enabled selection and optimization of desired third-order signal contributions based on all of the optical phases, polarizations, and pulse-timing schemes.

Although UTC coherences appear in two-quantum, third-order 2D FTOPT measurements with most polarization combinations, their analysis is challenging because their signal contributions cannot be separated easily. One study concluded that the UTC feature can be modeled using an EIS term,[20] but third-order measurements have not provided detailed information about the phenomenon. Through experiments and simulations, here we show that the dominant mechanism giving rise to the UTC remains EIS for fifth-order measurements, and our results show that even higher-order correlations (above fifth-order) result in collisional broadening and energy renormalization of the UTC.

Here, we gain insights into the inhomogeneity and dephasing characteristics of two-quantum coherences by measuring 2D spectra of fifth-order rephasing (photon echo) signals. Similar measurements were performed in the IR to study a very different phenomenon (molecular vibrational anharmonicity);[22] maintaining the required phase stability is more difficult in the optical regime. Independent polarization control of the two fields that create the two-quantum coherence is needed to select between biexciton and UTC coherences. We therefore use separate beams for those two fields, and we use a third beam for three additional field interactions. This

results in one of many unconventional beam arrangements needed for fully phase-coherent measurements at high orders. Therefore we have developed a versatile instrument, called the coherent optical laser beam recombination technique (COLBERT) spectrometer, to generate multiple beams in specified geometries with fully phase-coherent fields.[23]

The paper is arranged as follows. In Sec. II, we describe the sample and how multidimensional spectroscopy performed using the COLBERT spectrometer probes exciton interactions in quantum wells, and we show spectra measured using three different polarization configurations that show biexciton and UTC signals together and separately. In Sec. III, we describe two theoretical approaches used to understand and predict the signatures of MBIs in multidimensional spectroscopic measurements of GaAs quantum wells. Finally, in Sec. IV, the relative importance of specific many-body interactions in the UTC dynamics and the sensitivity of the fifth-order measurements to these interactions are discussed by comparing the measured results to the predictions of the two theoretical models.

II. EXPERIMENT

We performed the measurements using the COLBERT spectrometer with the beams in the Y-shaped formation illustrated in Fig. 1. The optical setup was fully phase stable because all the beams traversed a common set of optics.[23] Although five fields interacted with the sample and many field parameters could have been varied, in the present measurements only the time period (τ) between the conjugate beams ($\mathbf{E}_a$ and $\mathbf{E}_b$) and the final beam ($\mathbf{E}_c$) was scanned. The final three field interactions—all due to one laser beam, $\mathbf{E}_c$—converted the two-quantum coherences created by beams $\mathbf{E}_a$ and $\mathbf{E}_b$ to radiative one-quantum coherences. 2D scans were performed by varying τ (maintaining constant optical phases of all fields at a selected reference frequency) and at each step interferometrically detecting the signal in a spectrometer after overlapping it with the reference field. Fourier transformation with respect to the delay time yielded 2D spectra as functions of the two-quantum frequency and the emission frequency. The

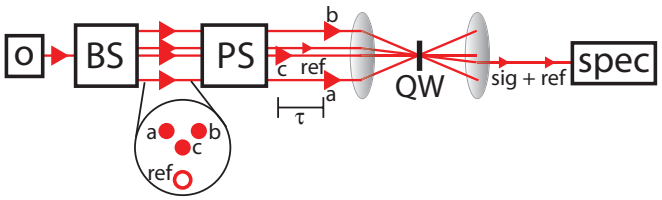

FIG. 1. (Color online) Block diagram of the COLBERT spectrometer and the multiple fields that it generates and controls for the present experiments. A Ti:sapphire oscillator (o) creates femtosecond pulses in a single beam. The beam shaper (BS) transforms this beam into four beams arranged in a Y-shaped geometry. The pulse shaper (PS) controls the delays and phases of the pulses, which are then focused to the sample (QW). Fields $\mathbf{E}_a$ and $\mathbf{E}_b$ interact with the sample first, followed after a variable delay (τ) by field $\mathbf{E}_c$ which interacts three times to generate a phase-matched signal in the $3\mathbf{k}_c$-$\mathbf{k}_a$-$\mathbf{k}_b$ direction. The resulting signal is overlapped with a weak reference field $\mathbf{E}_{ref}$ and is heterodyne detected by the CCD spectrometer (spec).

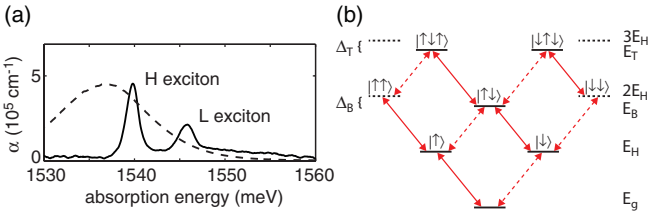

FIG. 2. (Color online) Spectra and energy levels of the exciton states of GaAs. (a) Linear absorption spectrum (solid) and optical pulse spectra (dashed). The pulse spectra primarily excite the H exciton. We do not observe signals involving the L exciton or the continuum. (b) The quasi-particle energy level scheme includes the energies of the ground state (E_g) and H excitons (E_H). The energy of the biexciton state is redshifted by its binding energy (Δ_B) from the two-exciton energy: $E_B = 2E_H - \Delta_B$. The triexciton energy is similarly shifted from the three-exciton energy by its binding energy: $E_T = 3E_H - \Delta_T$. Full and dashed lines indicate right and left circularly polarized excitation. No transitions are indicated to the unbound three-exciton levels because their signatures have not been observed.[24]

carrier frequency and global phase were calibrated and phase cycling was employed using established procedures.[19,20,23,24]

A Ti:sapphire oscillator with a repetition rate of 92.5 MHz was adjusted to create nearly transform-limited pulses of 150 fs duration, centered at 1534 meV, with a FWHM of about 11 meV. The sample consisted of ten layers of 10 nm thick GaAs, separated by 10 nm thick $Al_{0.3}Ga_{0.7}As$ barriers, and it was cooled to a temperature below 10 K in a cold-finger cryostat. The heavy-hole (H) and light-hole (L) exciton resonance energies are 1539 and 1546 meV, respectively. The pulse spectrum shown in Fig. 2(a) was set so that only resonances involving H excitons appeared; resonances involving L excitons, such as mixed biexcitons, were suppressed. Moreover, the pulses did not significantly excite the continuum of unbound electron-hole states which appear at energies greater than the L exciton. We use a quasi-particle representation in Fig. 2(b) to illustrate the energy levels and selection rules. Right-circularly (dashed lines) and left-circularly (full lines) polarized fields excite spin-down (>) and spin-up (<) H excitons, respectively, with energy E_H. Opposite polarized conjugate fields form a biexciton–ground-state two-quantum coherence with energy E_B, while conjugate fields with the same circular polarization form a UTC–ground-state two-quantum coherence with energy $2E_H$. The energy difference between these two levels is the biexciton binding energy, $\Delta_B = 2E_H - E_B = 1.0$ meV.[17] We also show the triexciton energy, redshifted from the three-exciton energy by its binding energy, $\Delta_T = 3E_H - E_T = 1.8$ meV,[24] because triexciton–biexciton emission pathways contribute to the signals.

The first spectra we present were measured using collinearly polarized pulses. Both biexciton and UTC coherent oscillations are measured during time interval τ in this polarization configuration since signals derived from both circular polarization components of each beam are present. The amplitude spectrum, Fig. 3(a), has a node between the two features, distorting them such that their peaks appear farther apart than their true energy separation. Multiexciton

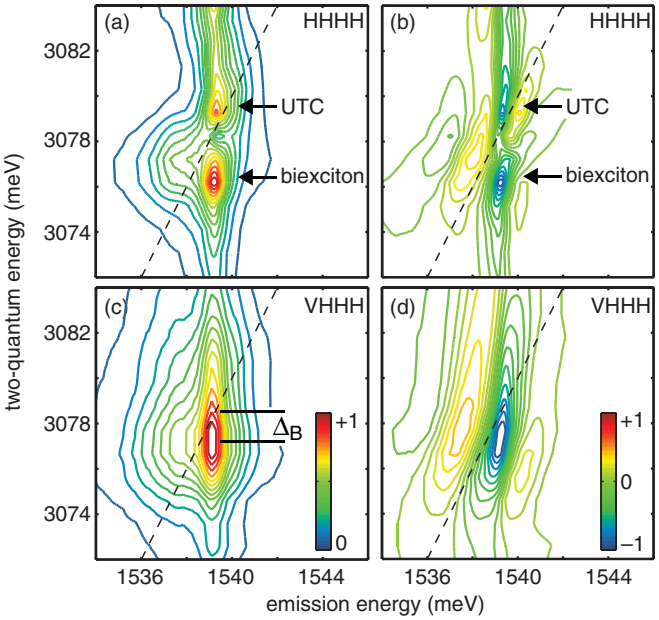

FIG. 3. (Color online) Experimental 2D spectra for two polarization configurations. Dashed lines are two-quantum diagonals, $E_{2Q} = 2E_{\text{emit}}$. Amplitude (a) and real (b) spectra for colinear polarized fields show both two-quantum coherences. Cross-linear polarized fields suppress UTC coherences to isolate biexciton coherences in the amplitude (c) and real (d) spectra.

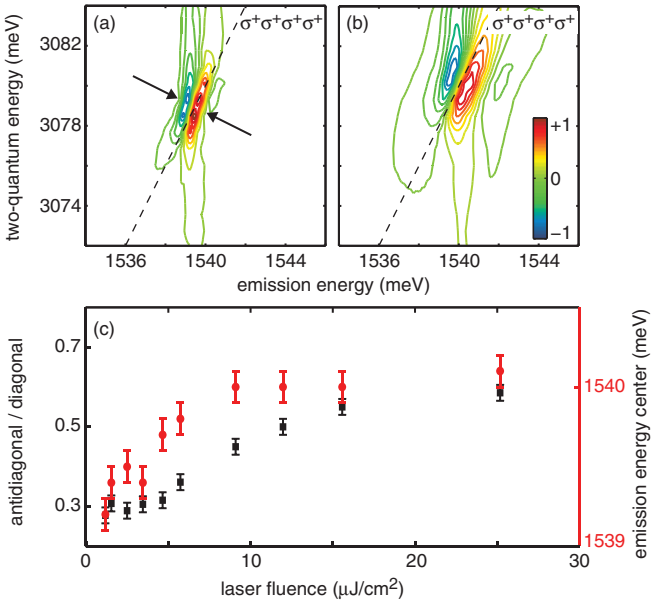

FIG. 4. (Color online) Real spectra for cocircular polarized fields at low (a) and high (b) powers. The arrows indicate the antidiagonal, and the dashed lines indicate the two-quantum diagonals. (c) Result of ten measurements with varying powers. The peak becomes more homogeneously broadened (black squares) and blueshifts (red circles) as the fluence increases. A fluence of 4 μJ/cm^2 corresponds to the carrier density where absorption saturation begins to occur, $\sim 10^{11}$ exciton/cm^2/well.

emission is visible as a redshifted shoulder on the biexciton peak. The shoulder is due to the energy differences between the radiative exciton–ground-state coherence ($|H\rangle\langle g|$) and the other radiative coherences: biexciton–exciton ($|HH\rangle\langle H|$) and triexciton–biexciton ($|HHH\rangle\langle HH|$). Because the pathways overlap, we cannot separate the different emission energies. The real part of the spectrum, Fig. 3(b), shows that the biexciton coherence and the UTC coherence are out of phase and interfere destructively. This results in an entwined line shape and makes analysis difficult.

In the cross-linear polarization measurement, all of the fields have horizontal polarization except field $\mathbf{E}_a$, which has vertical polarization; we measure identical spectra if only field $\mathbf{E}_b$ is vertically polarized or if only field $\mathbf{E}_c$ is vertically polarized. The main feature due to biexciton coherences in the amplitude spectrum, Fig. 3(c), is shifted below the diagonal by an amount equal to the biexciton–ground-state binding energy (Δ_B), which we measure to be 1.2 ± 0.2 meV. The redshifted shoulder due to multiexciton emission is again present. The two-quantum linewidth appears to have increased relative to that in the colinear polarized spectrum. Unlike in third-order rephasing spectra of single excitons where the nodes are parallel to the diagonal,[12,13,19] the nodes in Fig. 3(d) are tilted.

Figures 4(a) and 4(b) are spectra of only UTC measured using cocircular polarization at low (1 μJ/cm^2) and high (25 μJ/cm^2) laser fluence, respectively. In both spectra, the lineshapes are dispersive and the nodes are again not parallel to the diagonal. The diagonally elongated peak shows less homogeneous broadening (antidiagonal width) at low powers than at high powers. The peak also blueshifts by about 1 meV along the two-quantum diagonal at higher powers.

To investigate these changes further, we measured cocircular spectra at ten different fluences. Figure 4(c) shows how the linewidth ratio (antidiagonal/diagonal) and the position of the emission energy maximum change. As the fluence increases, the diagonal linewidth increases 14% from 3.6 to 4.1 meV and the antidiagonal linewidth increases 140% from 1.0 to 2.4 meV. The diagonal linewidth is strongly determined by static disorder (inhomogeneity) due to well-width fluctuations and defects;[25] these parameters do not change with pulse fluence. On the other hand, the antidiagonal linewidth provides a measure of the homogeneous dephasing rate. At higher fluences, more excitons are excited, more scattering occurs, and therefore the coherent signal dephases more quickly.

III. THEORY

Nonlinear optical signals involving the interactions between a series of femtosecond laser pulses and a sample can be described in terms of the time evolution of the system density matrix. At least three distinct constructs are often employed to model the system and the electric field interactions. In a first approximation, a set of double-sided Feynman diagrams can account for the possible light-matter interactions and time orderings of the electric fields with the system eigenstates.[26,27] This method has been called the sum-over-states approach, and, because it cannot include any exciton interaction mechanisms, it is a valuable reference for the result expected in the absence of MBIs.

Other methods can include exciton interaction mechanisms. The signatures in 2D FTOPT spectra of MBIs among excitons

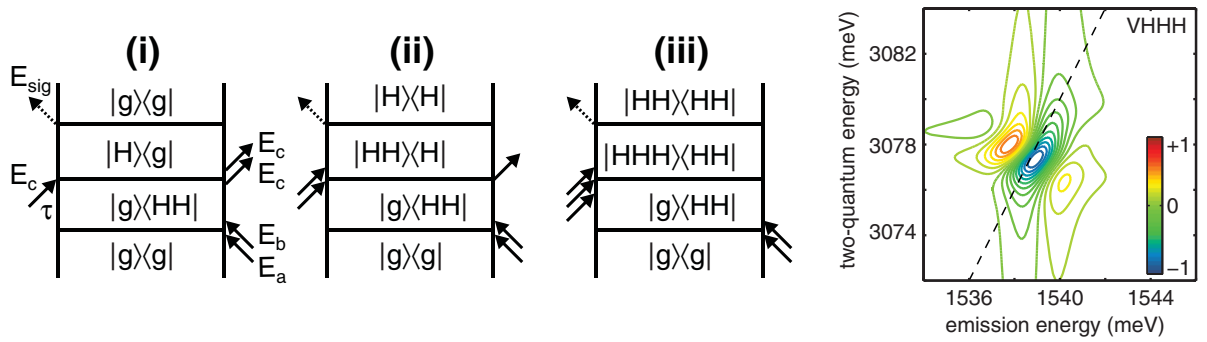

FIG. 5. (Color online) Double-sided Feynman diagrams relevant to the cross-linear polarization case in the sum-over-states model. Diagrams (i), (ii), and (iii) illustrate exciton-ground-state, biexciton-exciton, and triexciton-biexciton emission pathways, respectively. Simulation for cross-linear polarization spectrum using the sum-over-states model.

in semiconductor quantum wells have been simulated using phenomenological[11,17] and microscopic first-principles[12,28,29] calculations. The former treat the quantum well as a simple few-level system (meaning that it begins with the same isolated states used in the sum-over-states approach) and then includes phenomenological terms to represent the MBIs, including any required binding energies, while the latter considers only the band structure of the semiconductor quantum well and the Coulomb coupling to generate the excitons, the multiexcitons, and the MBIs. The differences and similarities between the two approaches have been detailed elsewhere.[30] While the microscopic calculation provides details about MBIs—such as the two-exciton memory function[31] and exciton binding energies[29]—that the phenomenological model cannot, the phenomenological model allows researchers to identify the signatures of specific MBIs (EIS, EID, LFEs, and bound multiexciton states) in 2D FTOPT using more tractable computations with ready physical interpretations.

As in third-order 2D FTOPT,[12] MBIs can dramatically modify the lineshapes, frequencies, and phases of peaks in fifth-order 2D FTOPT. Microscopic calculations of fifth-order one-quantum signals have been reported,[32,33] but the manifestations of MBIs in 2D FTOPT have not been discussed. Here, we identify the signatures of MBIs in fifth-order 2D FTOPT using a phenomenological model based on the two-level Bloch equations, which we have extended to four levels to include the bound biexciton and bound triexciton states. The purpose of these calculations is not to simulate the signal rigorously using first-principle equations,[21,34,35] but to identify which many-body interactions contribute to the experimental spectra. After briefly describing the sum-over-states approach and its results, we detail the derivation of the phenomenological model and then describe the 2D spectra predicted under a variety of conditions.

A. Sum-over-states model

The sum-over-states model[22,36] treats the excitons and multiexcitons as isolated states and then accounts for the possible interactions with the electric field in a perturbative fashion given by the order of the nonlinear optical susceptibility, $\chi^{(n)}$. In this approach, we include four states: the ground $|g\rangle$, exciton $|H\rangle$, biexciton $|HH\rangle$, and triexciton $|HHH\rangle$ states, and five coherent interactions with the incident electric fields to generate the fifth-order signal as given by

$$E_{\mathrm{sig}}^{(5)} \propto \chi^{(5)} E_c^3 E_b^* E_a^*. \tag{1}$$

The three relevant double-sided Feynman diagrams are illustrated in Fig. 5, where all three diagrams contain two-quantum coherences ($|g\rangle\langle HH|$) during the scanned time period (τ), but contain different coherences during the emitted time period. The weighting of each diagram is given by the number of different time-orderings of the last three field interactions; diagrams (i) and (ii) have three possible paths, while diagram (iii) has only one possible path. In this simulation, we assumed that the dipole moments connecting the various states are equal.[30]

This simplified approach reproduces only the features due to noninteracting particles. The sum-over-states model for cross-circular polarization results in the spectrum shown in Fig. 5. Both multiexciton emission pathways [pathways (ii) and (iii)] are included in this spectrum using the measured binding energies. This model reproduces the number of nodes, their locations, and their relative intensities, but it does not reproduce the slight nodal tilts or the vertical elongation present in the experiment. The nodes are also blueshifted slightly up the two-quantum axis from their experimental locations.

Although this approach results in a spectrum that qualitatively reproduces the cross-linear polarization experiment, since the sum-over-states model does not include the unbound two-exciton correlations or the interactions that produce them, it does not reproduce the UTC features in the colinear spectrum and it predicts no peak at all in the cocircular spectrum.

B. Phenomenological model

1. Derivation of coupled equations of motion

In the exciton basis, the density matrix and the Hamiltonian describe the ground state and each exciton or multiexciton state. An n-level system has a Hamiltonian with n diagonal matrix elements containing the energy of each state and its lifetime. The off-diagonal elements contain the electric field interactions and the dephasing parameters. For example, the four-level Hamiltonian given in Eq. (2) is used to represent the ground (g), H exciton (X), HH biexciton (B), and HHH triexciton (T) states. Optical transitions are allowed between states with ± 1 number of electron-hole pairs composing the

states such that

$$\hat{H}(t) = -i \begin{bmatrix} 0 & \Delta_l(t) - i\gamma_{Xg} & 0 & 0 \\ \Delta_l^*(t) + i\gamma_{Xg} & \epsilon_X - i\Gamma_X & \Delta_l(t) - i\gamma_{BX} & 0 \\ 0 & \Delta_l^*(t) + i\gamma_{BX} & \epsilon_B - i\Gamma_B & \Delta_l(t) - i\gamma_{TB} \\ 0 & 0 & \Delta_l^*(t) + i\gamma_{TB} & \epsilon_T - i\Gamma_T \end{bmatrix}, \tag{2}$$

where ϵ_α and Γ_α represent the energy and lifetime of state α, respectively, and $\gamma_{\beta\alpha}$ represents the dephasing of the off-diagonal matrix elements, where α and $\beta \in \{g, X, B, T\}$, and $\Delta_l(t) = \mu E_l(t)$ where μ is the transition dipole (equal for all the transitions[30]) and $E_l(t)$ is the electric field provided by a laser pulse as elaborated further below. We have set $\hbar = 1$. The density matrix for the case of the four-level system is given by

$$\rho = \begin{bmatrix} \rho_{gg} & \rho_{gX} & \rho_{gB} & \rho_{gT} \\ \rho_{Xg} & \rho_{XX} & \rho_{XB} & \rho_{XT} \\ \rho_{Bg} & \rho_{BX} & \rho_{BB} & \rho_{BT} \\ \rho_{Tg} & \rho_{TX} & \rho_{TB} & \rho_{TT} \end{bmatrix}, \tag{3}$$

where the time variable has been suppressed. The density matrix and the Hamiltonian are inserted into the quantum-Liouville equation, and a set of coupled differential equations are derived. Generalized diagonal density matrix elements derived from the quantum-Liouville equation describe the population dynamics,

$$\frac{d}{dt}\rho_{aa} = -\Gamma_{aa}\rho_{aa} + i[(\rho_{a,a-1} - \rho_{a+1,a})\Delta_l(t) - (\rho_{a-1,a} + \rho_{a,a+1})\Delta_l^*(t)], \tag{4}$$

and off-diagonal elements describe the coherence terms,

$$\frac{d}{dt}\rho_{ab} = -\gamma_{ab} + i[\omega_{ab}\rho_{ab} + (\rho_{aa} - \rho_{bb} + \rho_{a,b-1} - \rho_{a+1,b}) \times \Delta_l(t) + (-\rho_{bb} + \rho_{aa} - \rho_{a-1,b} + \rho_{a,b+1})\Delta_l^*(t)], \tag{5}$$

where $\omega_{ab} = \epsilon_a - \epsilon_b$. The equations can be solved through numerical integration techniques. Equations (4) and (5) are the optical Bloch equations.

The wave vector dependence is incorporated using a spatial Fourier expansion of the matrix elements to determine which components contribute to signals in a particular direction (the phase-matched direction).[37–40] Since the equations are not perturbative, in this discussion "order" refers to the spatial direction, not the susceptibility. In principle, the wave vector expansion of the density matrix elements can result in a large number of coupled equations. To keep the bookkeeping simple, here we use two beams with wave vectors $\mathbf{K} + \mathbf{k}$ and $\mathbf{K} - \mathbf{k}$, and the interaction with the system is written as

$$\Delta_l(t) = \mu E_-(t)e^{-i(\mathbf{K}-\mathbf{k})\cdot\mathbf{r}} + \mu E_+(t)e^{-i(\mathbf{K}+\mathbf{k})\cdot\mathbf{r}}, \tag{6}$$

where $E_+(t)$ and $E_-(t)$ are the electric fields in the $\mathbf{K} + \mathbf{k}$ and $\mathbf{K} - \mathbf{k}$ directions, respectively. Multiple interactions with the fields of these two wave vectors can produce signal in the fifth-order phase-matched direction given by

$$3(\mathbf{K} - \mathbf{k}) - 2(\mathbf{K} + \mathbf{k}) = \mathbf{K} - 5\mathbf{k}. \tag{7}$$

Describing the wave vectors of the two fields in this manner allows us to count spatial expansion orders easily. (The experimental geometry used differs only slightly in that the $\mathbf{K} + \mathbf{k}$ beam was split into two beams, each with a small additional wave-vector component perpendicular to the plane formed by $\mathbf{K}$ and $\mathbf{k}$, so that we could insert different polarizers into the two beams. The signal wave vector was the same as in Eq. (7) since the perpendicular wave-vector components cancelled.) The density matrix elements are then expanded in terms of these wave vectors:

$$\rho_{aa} = \sum_{A=-m}^{+m} \rho_{aa,A}e^{iA\mathbf{k}\cdot\mathbf{r}} \tag{8}$$

and

$$\rho_{ab} = \sum_{A=-m}^{+m} \rho_{ab,A}e^{i(|b-a|\mathbf{K}+A\mathbf{k})\cdot\mathbf{r}}. \tag{9}$$

In our approach, we truncate A at $\pm m$ using the desired spatial expansion order. As a consequence, any term with $|A| > 5$ is set to zero in the fifth-order expansion.

The standard approach is to assume the system begins in only the ground state: initially only $\rho_{gg,0}$ is nonzero. Elements $\rho_{Xg,\pm1}$ then acquire some nonzero value due to the light-matter coupling with $\rho_{gg,0}$. Subsequently, states coupled with $\rho_{Xg,\pm1}$ acquire nonzero values, and so forth. Because the equations are based on spatial expansion and not perturbation theory, elements that have higher-order expansion coefficients may couple to elements with lower-order expansion coefficients. For example, a first-order polarization $\rho_{Xg,+1}$ is coupled to zero-order populations through fields with $-\mathbf{k}$ wave vector component. A portion of the set of equations for the four-level system example is shown in Fig. 6. This hierarchy represents signals in positive-$\mathbf{k}$ directions where lower-order terms are sources for higher-order terms. The set of differential equations for signal in negative-$\mathbf{k}$ directions is represented by the same hierarchy except solid (dashed) lines represent multiplication by $\mu E_-(t)$ [$\mu E_+(t)$] and all elements have negative-$\mathbf{k}$ indices (for example, $\rho_{gX,-1}$ instead of $\rho_{gX,1}$). Not shown in Fig. 6 are the transitions for which higher-order terms are sources for lower-order terms. Representative equations for the fifth-order example include

$$\frac{d}{dt}\rho_{Xg,5} = [-\gamma_{Xg} + i\omega_{Xg}]\rho_{Xg,5} + i\mu[-E_-(t)\rho_{Bg,4} - E_+^*(t)\rho_{gg,4} + E_+^*(t)\rho_{XX,4}], \tag{10}$$

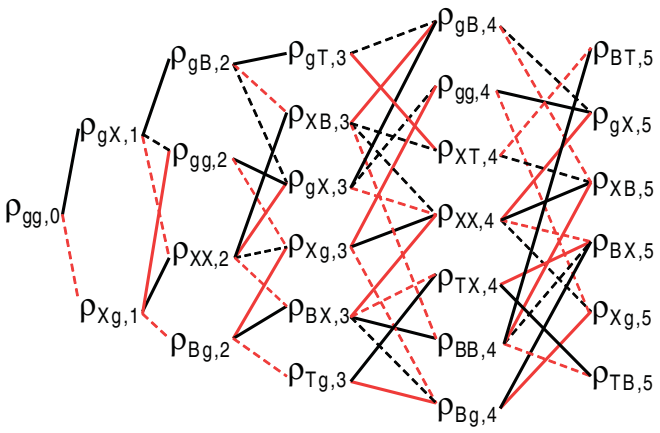

FIG. 6. (Color online) Hierarchy of differential equations for a portion of the fifth-order signal. Lower-order terms act as source terms for higher-order terms. Solid (dashed) lines represent multiplication of lower-order terms with $\mu E_+(t)$ [$\mu E_-(t)$] before addition to (black lines) or subtraction from (red lines) differential equation of higher-order terms. Some transitions—higher-order terms leading to lower-order terms—are not shown. For example, $\rho_{Xg,1}$ can lead to terms $\rho_{XX,2}$ (shown) and $\rho_{XX,0}$ (not shown).

$$\frac{d}{dt}\rho_{BX,5} = [-\gamma_{BX} + i\omega_{BX}]\rho_{BX,5} + i\mu[E_-^*(t)\rho_{Bg,4} - E_-(t)\rho_{TX,4} - E_+^*(t)\rho_{XX,4} + E_+^*(t)\rho_{BB,4}], \tag{11}$$

$$\frac{d}{dt}\rho_{Xg,3} = [-\gamma_{Xg}+i\omega_{Xg}]\rho_{Xg,3}+i\mu[E_+(t)\rho_{Bg,4}-E_-(t)\rho_{Bg,2} +E_-^*(t)(\rho_{XX,4} - \rho_{gg,4}) + E_+^*(t)(\rho_{XX,2} - \rho_{gg,2})], \tag{12}$$

$$\frac{d}{dt}\rho_{gX,1} = [-\gamma_{gX}+i\omega_{gX}]\rho_{gX,1}+i\mu[-E_+(t)\rho_{Bg,2} - E_-(t)\rho_{Bg,0} + E_-^*(t)(\rho_{XX,2} - \rho_{gg,2}) + E_+^*(t)(\rho_{XX,0}-\rho_{gg,0})], \tag{13}$$

and

$$\frac{d}{dt}\rho_{TB,5} = [-\gamma_{TB} + i\omega_{TB}]\rho_{TB,5} + i\mu[E_-^*(t)\rho_{TX,4} - E_+^*(t)\rho_{BB,4}]. \tag{14}$$

The terms $\rho_{Bg,0}$ and $\rho_{XX,0}$ in Eq. (13) are examples of terms that are not illustrated in Fig. 6.

Many-body interactions such as LFEs, EID, and EIS can be incorporated by inserting phenomenological terms. Although we do not use the phrase, the signals these terms produce have been called interaction-induced effects.[41,42] Local fields act as density-dependent source terms that modify the field interaction, and they are included by introducing a new electric field $\Delta(t)$ that includes the original electric field $\Delta_l(t)$ and the LFEs, as given by

$$\Delta(t) = \Delta_l(t) + \Delta^{\mathrm{LFE}}(t), \tag{15}$$

where

$$\Delta^{\mathrm{LFE}}(t) = \mu N l[\mu\rho_{Xg,-1}(t)e^{-i(\mathbf{K}-\mathbf{k})\cdot\mathbf{r}} + \mu\rho_{Xg,+1}(t)e^{-i(\mathbf{K}+\mathbf{k})\cdot\mathbf{r}}], \tag{16}$$

and l measures the strength of the effect. We neglect terms such as $\rho_{BX,\pm1}$, which, although they have the appropriate spatial order to be included in the total LFEs source, are orders of magnitude weaker because the multiexciton density is always far lower than the exciton density N.

The other MBIs, EIS, and EID, result from Coulomb coupling to populations of excited states. The phenomenological constants ω' and γ' are the EIS and EID terms, respectively. To the right side of Eq. (5), EID and EIS are added using $\frac{d}{dt}p_{ab}^{\mathrm{EI}}$, where

$$\frac{d}{dt}p_{ab}^{\mathrm{EI}} = (\gamma' + i\omega')N\sum_{c\in\{X,B,T\}} n_c p_{ab}. \tag{17}$$

Although the EID and EIS parameters likely depend on the choice of c (whether coupling involves excitons, biexcitons, or triexcitons), we show below that the signals measured in our experiments can be modeled without this complication; we use a single value for γ' or ω' which does not depend on the nature of the state involved. The spatial Fourier expansions of the density matrix elements, Eqs. (8) and (9), must be inserted into Eq. (17). Populations ($n_{c,\mathbf{q}'}$) with wave vector $\mathbf{q}'$ couple with polarizations ($p_{ab,\mathbf{q}-\mathbf{q}'}$) with wave vector $\mathbf{q}-\mathbf{q}'$ and act as source terms for polarizations ($p_{ab,\mathbf{q}}$) with wave vector $\mathbf{q}$ such that

$$\frac{d}{dt}p_{ab,\mathbf{q}}^{\mathrm{EI}} = (\gamma' + i\omega')N\sum_{c\in\{X,B,T\}} n_{c,\mathbf{r}}\, p_{ab,\mathbf{q}-\mathbf{q}'}. \tag{18}$$

In a fifth-order experiment, $n_{T,\mathbf{q}'}$ is zero for all orders of $\mathbf{k}$ so the summation is effectively over c, where $c \in \{X,B\}$. Proper selection of $n_{c,\mathbf{q}'}$ and $p_{ab,\mathbf{q}-\mathbf{q}'}$ is a tedious but straightforward algebraic exercise.

Including all three effects results in equations of motion with the following forms. Coherence terms have the form

$$\frac{d}{dt}\sum_A \rho_{ab,A} = \left[-\left(\gamma_{ab} + \gamma'_{ab}N\sum_{A,c}\rho_{cc,A}\right) + i\left(\omega_{ab} + \omega'_{ab}N\sum_{A,c}\rho_{cc,A}\right)\right]\sum_{A,c,d}\rho_{cd,A} + i\left(\sum_A \rho_{aa,A} + \sum_A \rho_{ab,A}\right)\Delta(t), \tag{19}$$

where $c,d \in \{X,B,T\}$, and population terms have the form

$$\frac{d}{dt}\sum_A \rho_{aa,A} = -\sum_A \Gamma_{aa}\rho_{aa,A} + i\sum_A \rho_{ab,A}\Delta(t), \tag{20}$$

where we can collect terms having the same spatial expansion order (given by the value of A) and equate them. Two elements from our fifth-order example are the complete equations for $\rho_{Xg,5}$ and $\rho_{gX,1}$,

$$\frac{d}{dt}\rho_{Xg,5} = [-\gamma_{Xg} + i\omega_{Xg}]\rho_{Xg,5} + i\mu[-E_-(t)\rho_{Bg,4} - E_+^*(t)\rho_{gg,4} + E_+^*(t)\rho_{XX,4}] + (\gamma' + i\omega')N[\rho_{Xg,1}(\rho_{XX,4} + \rho_{BB,4} + \rho_{TT,4}) + \rho_{Xg,3}(\rho_{XX,2} + \rho_{BB,2} + \rho_{TT,2}) + \rho_{Xg,5}(\rho_{XX,0} + \rho_{BB,0} + \rho_{TT,0})], \tag{21}$$

and

$$\begin{aligned}\frac{d}{dt}\rho_{gX,1} &= [-\gamma_{gX}+i\omega_{gX}]\rho_{gX,1}+i\mu[-E_+(t)\rho_{Bg,2}-E_-(t)\rho_{Bg,0}\\ &+E_-^*(t)(\rho_{XX,2}-\rho_{gg,2})+E_+^*(t)(\rho_{XX,0}-\rho_{gg,0})]\\ &+(\gamma'+i\omega')N[\rho_{gX,-3}(\rho_{XX,4}+\rho_{BB,4}+\rho_{TT,4})\\ &+\rho_{gX,-1}(\rho_{XX,2}+\rho_{BB,2}+\rho_{TT,2})\\ &+\rho_{gX,1}(\rho_{XX,0}+\rho_{BB,0}+\rho_{TT,0})\\ &+\rho_{gX,3}(\rho_{XX,-2}+\rho_{BB,-2}+\rho_{TT,-2})\\ &+\rho_{gX,5}(\rho_{XX,-4}+\rho_{BB,-4}+\rho_{TT,-4})]. \end{aligned} \quad (22)$$

In Eq. (22), for $\rho_{gX,1}$, there are no terms in the $\rho_{gX,-5}$ direction because—even though the resulting signal is fifth-order—such terms would require sixth-order populations, $\rho_{XX,6}$ for example, which are excluded from our spatial expansion. Similarly, there are no terms due to $\rho_{Xg,-1}$ in Eq. (21).

The simplified equations, Eqs. (19) and (20), show that the EID and EIS terms provide density-dependent modifications to the real and imaginary parts, respectively, of coherences. This result is the same for the third-order modified optical Bloch equations.[10] Extended to fifth order, the modified optical Bloch equations contain more states and terms that couple the differential equations, but the physical intuition underlying the equations remains largely the same.

Finally, in this model, inhomogenous broadening can be incorporated by summing over different configurations of the Hamiltonian; in other words, small spreads in energies for ϵ_X, ϵ_B, and ϵ_T could be used. We investigated the effect of including inhomogeneous broadening and concluded that the effect was of minor importance, as suggested by the experiments. Therefore no inhomogeneity was included in the simulated spectra presented here.

2. Computation details

Each spectrum was calculated by solving the set of coupled differential equations using an adaptive Runge-Kutta algorithm in approximately 15 minutes on a computer that had a 2-GHz processor and 2-Gb RAM. The two-quantum time dimension was calculated in 500 steps over 10 ps, while the emission time dimension was calculated in about 1000 steps over 50 ps. The adaptive algorithm uses small (large) time steps when the oscillation amplitude is large (small), so the emission dimension was interpolated to a linearly spaced time axis after the signal was computed. The resulting time-time matrix was fast Fourier transformed to yield the 2D spectrum. Each spectrum was normalized and its amplitude and real parts were plotted using sixteen contours. Red colors are positive contours, while blue colors are negative contours.

We used a value of 15 D for the transition dipole moments between states.[30] The LFE parameter value (unitless) and the EID and EIS parameter values γ' and ω' (THz/m^3) were determined through comparison of the calculated and measured spectra. We used pulse fluences appropriate for the experiments.

3. Calculated spectra

Two-dimensional spectra were calculated by first summing the fifth-order polarizations that contribute to signal in the $3(\mathbf{K}-\mathbf{k})-2(\mathbf{K}+\mathbf{k})=\mathbf{K}-5\mathbf{k}$ direction,

$$p_{\text{total}}(t_{2Q},t_{\text{emait}}) = p_{Xg,-5}+p_{BX,-5}+p_{TB,-5}, \quad (23)$$

and then converting the resulting spectra to energy units (meV) after taking the 2D Fourier transform,

$$S(E_{2Q},E_{\text{emit}}) = \mathscr{F}[p_{\text{total}}(t_{2Q},t_{\text{emit}})]. \quad (24)$$

In this signal direction, a two-quantum rephasing scan occurs when the E_- interaction—the positive wave-vector field contributing $3\mathbf{k}_c$—occurs last; E_- is held at time zero, while E_+—the field from time-coincident pulses contributing $-\mathbf{k}_a-\mathbf{k}_b$ is scanned backward from time zero to earlier times. Polarization selection rules were enforced in the calculations by setting density matrix terms involving biexciton and triexciton states to zero for cocircular calculations (light-hole excitons, mixed biexciton and triexciton states involving light-hole excitons, and continuum contributions were not considered).

As discussed earlier, under the cross-linear polarization condition, EID and EIS are suppressed because exciton population gratings are not produced. On the other hand, LFEs are not suppressed and are therefore expected to cause phase shifts and lineshape changes in the heavy-hole biexciton peak. We first calculated a spectrum in which no MBIs were included; neither the amplitude of the spectrum in Fig. 7(a) nor its real part in Fig. 7(b) reproduce the experiment. The spectrum calculated after including a small LFE contribution ($l=0.05$), Fig. 7(c), largely reproduces the experimentally observed spectrum shown in Fig. 3(d).

For cocircular scans, all three MBIs could, in principle, contribute to the observed signal. To determine which MBIs lead to the formation of the two-quantum signals, we first calculated spectra using each term individually. The results are shown in Fig. 8. When no MBIs are included, no signal is observed (not shown). In the real part of the 2D spectrum, EID [see Fig. 8(a)] produces a mostly absorptive line shape while LFE [see Fig. 8(b)] and EIS [see Fig. 8(c)] produce dispersive line shapes, although with different phase shifts from those observed experimentally.

Compared to the experimental spectrum in Fig. 4, the calculated spectra in Fig. 8 show that EIS is the dominant MBI leading to the UTC two-quantum signal. However, the match can be improved by including a small EID contribution as shown in Fig. 9, where the spectra were calculated using $\gamma'=5\times10^{-25}$ THz/m^3, $\omega'=5\times10^{-24}$ THz/m^3. The spectra displayed in Figs. 9(a) and 9(b) were simulated at low and high fluences corresponding to carrier densities of 3×10^{10} excitons/cm^2/well (or, $N\gamma'=0.02$ THz and $N\omega'=0.2$ THz) and 7×10^{11} excitons/cm^2/well, respectively. The differences between these two spectra and their experimental counterparts in Figs. 4(a) and 4(b) are minimal.

IV. DISCUSSION

The tilts, elongations, and energy shifts in the measured spectra all indicate the presence of many-body interactions beyond the pair interactions necessary for the two-quantum peaks to appear at all. We use two theoretical models to help understand these subtle spectral features.

Although calculations using the sum-over-states method for cross-linear polarization result in a spectrum that qualitatively

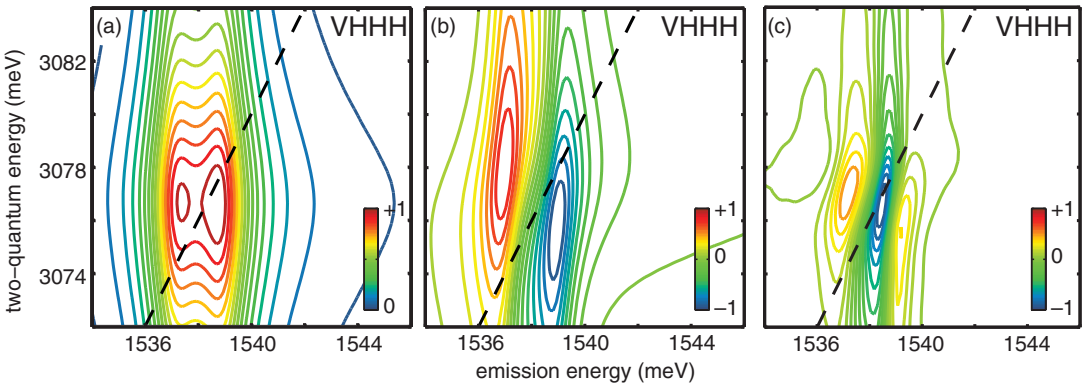

FIG. 7. (Color online) Cross-linear two-quantum rephasing spectra simulated using the phenomenological model. All four levels are included, but $\gamma' = \omega' = l = 0$ for (a) and (b), and the carrier density matched that of the experiment. Neither the amplitude spectrum, (a) nor the real part of the spectrum, (b) match the experimentally observed spectrum. (c) Inclusion of LFE ($l = 0.05$) better reproduces the experimental spectrum.

reproduces the nodes and the relative peak intensities for the multiexciton features, there are several deviations from the experiment. The multiexciton emission feature is blueshifted from its experimental location; the nodes are not tilted; and there is no vertical elongation. Moreover, the sum-over-states model could not reproduce the UTC features in the colinear and cocircular spectra.

The phenomenological model provided a better match to the cross-linear experiment and could generate convincing cocircular polarization spectra as well. The cross-linear spectrum, Fig. 7(c), does not include EID or EIS because they are suppressed in this polarization scheme.[13,20] However, LFEs can still contribute to the signal, and their inclusion stretches the spectrum vertically and tilts the nodes, yielding a better match to the experimental spectrum shown in Fig. 3. For the cocircular spectra in Figs. 9(a) and 9(b), all three MBIs may contribute to the two-quantum coherence and its rephasing. Comparing to the experimental 2D spectra, the cocircular features are reproduced mostly by EIS but cannot be reproduced without a small EID contribution to cause the vertical stretching in the node of the real spectrum. Although the phenomenological approach does not capture the many-body interactions in the most sophisticated manner, it provides important guidance to the origins of characteristic lineshapes

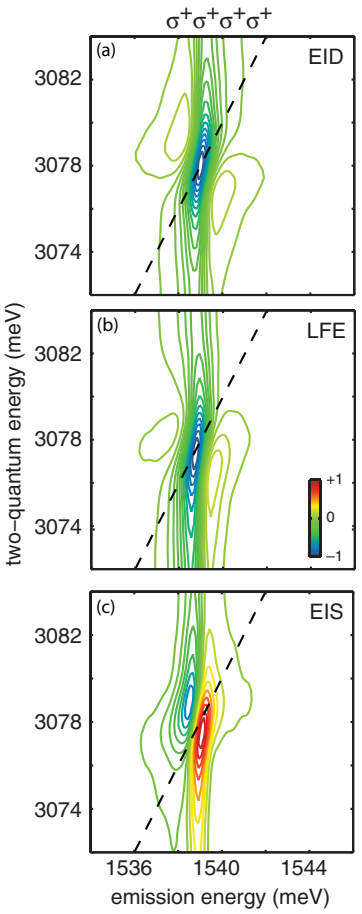

FIG. 8. (Color online) Calculated cocircular two-quantum rephasing real spectra using single MBI contributions. Only the ground and one single-exciton states are included, and the exciton density matches that of the lowest-fluence spectrum. Calculations were performed with (a) only EID: $\gamma' = 0.5 \times 10^{-24}$ THz/m^3, $\omega' = 0$, and $l = 0$; (b) only LFEs: $\gamma' = 0$, $\omega' = 0$, and $l = 5$; and (c) only EIS: $\gamma' = 0$, $\omega' = 5 \times 10^{-24}$ THz/m^3, and $l = 0$.

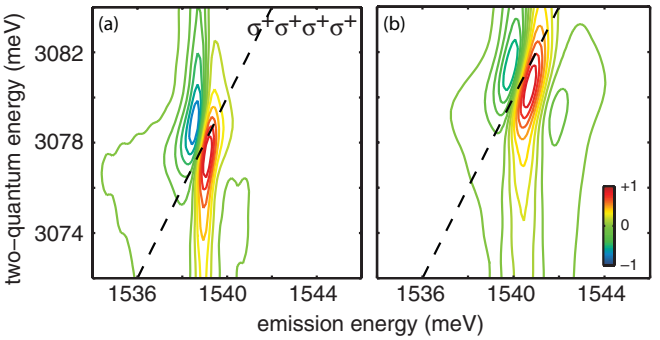

FIG. 9. (Color online) Calculated cocircular two-quantum rephasing real spectra using multiple MBI contributions; MBI values given in the text. EIS is largely responsible for the feature in (a) and (b) at the fluences of 1 μJ/cm^2 and 11 μJ/cm^2, respectively. Including small amounts of EID reproduced the experimental spectra better than including only the EIS interaction.

in 2D spectra. Specifically, the calculated and observed line shapes indicate that nonbinding Coulomb interactions that give rise to two-exciton coherences result largely in phase shifts of the coherences, evident in the dispersive nature of the peak. The line shapes also indicate the relative magnitudes of the EIS and EID effects.

Using the same phenomenological parameters, the peak blueshifts and broadens at higher fluences because—as in the experiment—the signal is not limited to fifth-order (in the susceptibility) contributions; extra interactions from a single beam (for example, $+\mathbf{k}_i - \mathbf{k}_i$) can contribute at high fluences. The blue shift and the broadening of the UTC are reproduced for high excitation powers in the phenomenological model. Using the same parameters for γ' and ω', 2D spectra calculated at low and high excitation fluences produced the power dependence of the excitation-induced energy shift and broadening, as shown in Fig. 4. Both the experimental and theoretical results indicate that higher-order susceptibility (beyond fifth-order susceptibility) contributions are present in the signal at high fluences. Because the phenomenological model is based on the spatial expansion and not the perturbative sum-over-states theory, the calculations are able to replicate qualitatively the power dependence of the excitation-induced shifts and broadening. However, since the phenomenological model does not contain an absorption saturation mechanism arising from the many-body interactions, the fluence-dependent results cannot be reproduced quantitatively. The simulations show that the fifth-order measurements provide sensitive indicators of two-exciton interactions, and they add to the insights offered by third-order spectroscopy.

V. CONCLUSIONS

In this study, we used the COLBERT spectrometer to measure fifth-order rephasing of two-quantum signals in GaAs quantum wells. We isolated biexciton coherences and measured the biexciton binding energy using cross-linear polarized fields. The binding energy and two-quantum linewidth are very similar to those measured using third-order signals at fluences about an order of magnitude lower than those used here.[17,20] In contrast, an analysis of a series of spectra measured using cocircular polarized fields indicated that the UTC coherences dephase more rapidly and blueshift with increasing carrier density. These variations are necessarily the result of interactions above fifth order in the susceptibility. More generally, any variation in the signal (other than a change of amplitude) for a given phase-matching geometry is necessarily the result of higher-order interactions than the minimum order that results in signal in the phase-matched direction. Removing the two-quantum inhomogeneous dephasing—which was valuable in this work to isolate and study the homogeneous dephasing characteristics of the UTC—is only possible in measurements using at least five light-matter interactions. Simulations showed that LFEs modified the biexciton coherence and that the UTC coherence was largely due to EIS. Comparison among the sum-over-states model, the phenomenological model, and the experimental data confirmed that many-body interactions play predominant roles in this sample at the excitation conditions explored, and they demonstrated that fifth-order 2D FTOPT spectral features are highly sensitive to many-body interactions in semiconductor nanostructures.

ACKNOWLEDGMENTS

D.B.T. was supported by the NDSEG and NSF graduate fellowship programs. We thank Katherine Stone and Shaul Mukamel for useful conversations, and we thank Steve Cundiff for providing the sample. This work was supported in part by NSF Grant CHE-0616939.

*Present address: Department of Chemistry and Centre for Quantum Information and Quantum Control, 80 St. George Street, University of Toronto, Toronto, Ontario, Canada M5S 3H6.

†kanelson@mit.edu

[1] G. H. Wannier, Phys. Rev. **52**, 191 (1937).

[2] R. C. Miller, D. A. Kleinman, W. T. Tsang, and A. C. Gossard, Phys. Rev. B **24**, 1134 (1981).

[3] S. W. Koch, M. Kira, G. Khitrova, and H. M. Gibbs, Nat. Mater. **5**, 523 (2006).

[4] S. T. Cundiff, Opt. Express **16**, 4639 (2008).

[5] T. Meier, P. Thomas, and S. Koch, *Coherent Semiconductor Optics* (Springer-Verlag, Berlin, 2007).

[6] K. Leo, M. Wegener, J. Shah, D. S. Chemla, E. Gobel, T. Damen, S. Schmitt-Rink, and W. Schäfer, Phys. Rev. Lett. **65**, 1340 (1990).

[7] M. Wegener, D. S. Chemla, S. Schmitt-Rink, and W. Schafer, Phys. Rev. A **42**, 5675 (1990).

[8] D. S. Chemla and J. Shah, Nature (London) **411**, 549 (2001).

[9] H. Wang, K. Ferrio, D. G. Steel, Y. Hu, R. Binder, and S. Koch, Phys. Rev. Lett. **71**, 1261 (1993).

[10] J. M. Shacklette and S. T. Cundiff, Phys. Rev. B **66**, 045309 (2002).

[11] X. Li, T. Zhang, C. N. Borca, and S. T. Cundiff, Phys. Rev. Lett. **96**, 057406 (2006).

[12] T. Zhang, I. Kuznetsova, T. Meier, X. Li, R. P. Mirin, P. Thomas, and S. T. Cundiff, Proc. Natl. Acad. Sci. USA **104**, 14227 (2007).

[13] A. D. Bristow, D. Karaiskaj, X. Dai, R. P. Mirin, and S. T. Cundiff, Phys. Rev. B **79**, 161305(R) (2009).

[14] R. C. Miller, D. A. Kleinman, A. C. Gossard, and O. Munteanu, Phys. Rev. B **25**, 6545 (1982).

[15] V. I. Klimov, A. A. Mikhailovsky, S. Xu, A. Malko, J. A. Hollingsworth, C. A. Leatherdale, H. Eisler, and M. G. Bawendi, Science **290**, 314 (2000).

[16] T. Hornung, J. C. Vaughan, T. Feurer, and K. A. Nelson, Opt. Lett. **29**, 2052 (2004).

[17] K. W. Stone, K. Gundogdu, D. B. Turner, X. Li, S. T. Cundiff, and K. A. Nelson, Science **324**, 1169 (2009).

[18] A. D. Bristow, D. Karaiskaj, X. Dai, T. Zhang, C. Carlsson, K. R. Hagen, R. Jimenez, and S. T. Cundiff, Rev. Sci. Instrum. **80**, 073108 (2009).

[19]D. B. Turner, K. W. Stone, K. Gundogdu, and K. A. Nelson, J. Chem. Phys. **131**, 144510 (2009).
[20]K. W. Stone, D. B. Turner, K. Gundogdu, S. T. Cundiff, and K. A. Nelson, Acc. Chem. Res. **42**, 1452 (2009).
[21]D. Karaiskaj, A. D. Bristow, L. Yang, X. Dai, R. P. Mirin, S. Mukamel, and S. T. Cundiff, Phys. Rev. Lett. **104**, 117401 (2010).
[22]E. C. Fulmer, F. Ding, P. Mukherjee, and M. T. Zanni, Phys. Rev. Lett. **94**, 067402 (2005).
[23]D. B. Turner, K. W. Stone, K. Gundogdu, and K. A. Nelson, Rev. Sci. Instrum. **82**, 081301 (2011).
[24]D. B. Turner and K. A. Nelson, Nature (London) **466**, 1089 (2010).
[25]M. E. Siemens, G. Moody, H. Li, A. D. Bristow, and S. T. Cundiff, Opt. Express **18**, 17699 (2010).
[26]S. Mukamel, Annu. Rev. Phys. Chem. **51**, 691 (2000).
[27]M. Cho, Chem. Rev. **108**, 1331 (2008).
[28]I. Kuznetsova, T. Meier, S. T. Cundiff, and P. Thomas, Phys. Rev. B **76**, 153301 (2007).
[29]L. Yang and S. Mukamel, Phys. Rev. Lett. **100**, 057402 (2008).
[30]N. H. Kwong, I. Rumyantsev, R. Binder, and A. L. Smirl, Phys. Rev. B **72**, 235312 (2005).
[31]R. Takayama, N. H. Kwong, I. Rumyantsev, M. Kuwata-Gonokami, and R. Binder, Eur. Phys. J. B **25**, 445 (2002).
[32]S. R. Bolton, U. Neukirch, L. Sham, D. Chemla, and V. Axt, Phys. Rev. Lett. **85**, 2002 (2000).
[33]H. G. Breunig, T. Voss, I. Rückmann, J. Gutowski, V. M. Axt, and T. Kuhn, J. Opt. Soc. Am. B **20**, 1769 (2003).
[34]L. Yang and S. Mukamel, Phys. Rev. Lett. **100**, 057402 (2008).
[35]R. P. Smith, J. K. Wahlstrand, A. C. Funk, R. P. Mirin, S. T. Cundiff, J. T. Steiner, M. Schafer, M. Kira, and S. W. Koch, Phys. Rev. Lett. **104**, 247401 (2010).
[36]S. Mukamel, *Principles of Nonlinear Optical Spectroscopy* (Oxford University Press, New York, 1995).
[37]M. Lindberg, R. Binder, and S. W. Koch, Phys. Rev. A **45**, 1865 (1992).
[38]V. M. Axt and A. Stahl, Z. Phys. B **93**, 195 (1994).
[39]V. M. Axt and A. Stahl, Z. Phys. B **93**, 205 (1994).
[40]M. Lindberg, Y. Z. Hu, R. Binder, and S. W. Koch, Phys. Rev. B **50**, 18060 (1994).
[41]H. P. Wagner, A. Schätz, W. Langbein, J. M. Hvam, and A. L. Smirl, Phys. Rev. B **60**, 4454 (1999).
[42]J. Shah, *Ultrafast Spectroscopy of Semiconductors and Semiconductor Nanostructures* (Springer-Verlag, Berlin, 1999).